






# Isochrons in Injection Locked Photonic Oscillators: A New Frontier for High-Precision Localization

Alireza Famili , Member, IEEE, Georgia Himona , Member, IEEE, Yannis Kominis , Angelos Stavrou , Senior Member, IEEE, and Vassilios Kovanis 

**Abstract**—For decades, high-accuracy localization has driven the interest of the research community. Recent cases include augmented reality (AR) and virtual reality (VR), indoor robotics, and drone applications, which have led to the emergence of subcentimeter localization requirements. This study introduces a new approach for high-accuracy localization by utilizing *isochrons* in injection-locked tunable photonic oscillators, which we referred to as *Isochrons in Photonic Oscillators for Positioning* (IsoPos). The proposed paradigm shift takes advantage of photonic oscillators' radical frequency tunability and isochron structure to offer an innovative path for measuring the time of arrival (ToA). To achieve precise ToA measurements, IsoPos utilizes the phase shift induced by the incoming user signal. This shift is detected by analyzing the *phase response* of the receiver, i.e., a photonic oscillator, which is exclusively determined by its isochrons' structure. Furthermore, IsoPos uses the injection-locking method as well as the nonlinear properties of injection-locked photonic oscillators to achieve highly accurate phase synchronization between different positioning nodes. This contributes to a seamless 3-D localization devoid of errors caused by miss-synchronization. Our numerical simulations show that IsoPos achieves sub-1 mm accuracy in 3-D localization, surpassing the precision of existing positioning systems by at least one order of magnitude.

**Index Terms**—Injection locking, isochrons, localization, optimal anchor placement, photonic oscillators.

## I. INTRODUCTION

HIGH-PRECISION positioning is crucial for the development of indoor location-based services, such as emergency response, asset tracking, and autonomous robotic systems [1], [2], [3]. This is especially true for futuristic innovations, such as augmented reality (AR) and virtual reality (VR) [4]. Despite its crucial role in outdoor positioning and navigation, the Global Positioning System (GPS) encounters substantial limitations when used indoors [5]. This drawback mainly arises from environmental disturbances, including obstruction of satellite signals by buildings and other constructions. Even when GPS signals can be received indoors, they often lack the precision required to offer accurate positioning information [6]. As a result, GPS technology fails to deliver optimal performance when deployed indoors.

Received 7 June 2024; revised 4 October 2024; accepted 18 November 2024. Date of publication 21 November 2024; date of current version 17 December 2024. (Corresponding author: Alireza Famili.)

Alireza Famili was with the Department of Electrical and Computer Engineering, Virginia Tech, Arlington, VA 22203 USA. He is now with the WayWave Inc., Arlington, VA 22203 USA (e-mail: afamili@waywave.com).

Georgia Himona and Yannis Kominis are with the School of Applied Mathematical and Physical Sciences, National Technical University of Athens, 157 80 Athens, Greece (e-mail: ghimona@mail.ntua.gr; gkomin@central.ntua.gr).

Angelos Stavrou and Vassilios Kovanis are with the Department of Electrical and Computer Engineering, Virginia Tech, Arlington, VA 22203 USA (e-mail: angelos@vt.edu; vkovanis@vt.edu).

Digital Object Identifier 10.1109/JISPIN.2024.3504396

Vision-based techniques are frequently utilized as the primary technology for high-accuracy indoor localization/tracking due to their superior accuracy [7]. However, such methods face practical constraints, such as sensitivity to lighting conditions, occlusion, and high computational complexity. Hence, the effectiveness of vision-based approaches is limited, especially in visually impaired environments [8]. On the other hand, indoor positioning can also be achieved using ranging-based techniques, which involve utilizing radio frequency (RF) signals, among others. However, the accuracy of such technologies is contingent on the precision of time of arrival (ToA) or angle of arrival (AoA) measurements [9].

The accuracy of time measurements in ranging-based techniques hinges on measuring the RF signal after it has propagated through the environment. As a result, any degradation of signal quality, including the presence of noise, interference, and multipath fading, can significantly undermine the accuracy [10]. More importantly, limitations in receiver resolution drastically affect the accuracy of time measurements, thereby compromising the overall positioning accuracy [9]. Ultimately, existing systems for obtaining ToA suffer not only from these limitations but also lack a mechanism for measuring time with high resolution, resulting in inadequate localization accuracy.

One of the primary contributions of our work is the introduction of a novel timing mechanism called *Isochron Phase-Shift Timing* (IPT). IPT accurately calculates the phase shift determined by the isochrons' structure of an oscillator, enabling highly precise measurement of the ToA for incoming RF signals.

These precise time measurements play a crucial role in our 3-D localization system, **Isochrons in Photonic Oscillators for Positioning** (IsoPos). IsoPos utilizes these accurate ToA measurements to determine the distances between the user and each positioning node, which are later employed in a time difference of arrival (TDoA) scheme for localization. Another key contribution of our work is the introduction of a novel synchronization scheme, named **Injection-Locking Synchronization** (ILS). By leveraging ILS, we achieve precise synchronization among all the positioning nodes within IsoPos. This synchronization ensures that all nodes share the same clock for their measurements, further enhancing the accuracy and reliability of the system.

*Novel timing mechanism:* We introduce IPT, a novel approach for timing measurements with extremely high resolution leveraging *isochrons in photonic oscillators*. This approach is based on the concept of isochrons, originally introduced in the context of mathematical biology [11] and closely related to any robust self-sustained oscillation [12] occurring in physical or man-made systems. Such oscillations, also known as *limit cycles* in the terminology of the theory of dynamical systems, can serve as clocks with an extremely precise period. Their periods can be uniquely partitioned, not necessarily uniformly. Each partition is known as an isochron, and the union of these isochrons provides the subcycle time resolution. Isochrons dictate the system's phase response to external stimulations having the form of either a single pulse or a periodic pulsatile sequence. The phase response determines the induced phase shift of the clock due to an incoming pulse, in the first case, and the synchronization properties of the clock with the periodic sequence, in the second case [13]. It is only recently that these concepts have been introduced in photonic oscillators consisting of two coupled lasers in a controller–follower configuration [14], [15]. Such an optically injected laser is well-known for its tunable self-sustained oscillations and widely used in various applications including secure chaos [16] and quantum communications [17], [18]. The potential of utilizing photonic oscillators along with their isochrons' structure for precise time is discussed for the first time in this article.

*Novel synchronization approach:* We propose ILS, a novel synchronization approach that employs optical injection locking to implement precise time synchronization between different positioning anchors, a significant challenge in many available architectures. This synchronization ensures that all measured ToAs at various nodes have the same time bias compared to the user, enabling the utilization of the TDoA technique for 3-D positioning.

*Localization system:* We construct our localization system, IsoPos, by utilizing the IPT mechanism for timing and the ILS protocol for anchor synchronization. IsoPos offers greater flexibility compared to existing localization systems, as it provides time measurements with extremely high resolution independent of received RF signal characteristics. For the IPT mechanism in IsoPos, the transmitted signal from the user only triggers the system to generate excitation pulses, while ToA measurements are derived from the phase response of the photonic oscillators' behavior to these pulses, determined by the isochrons' structure.

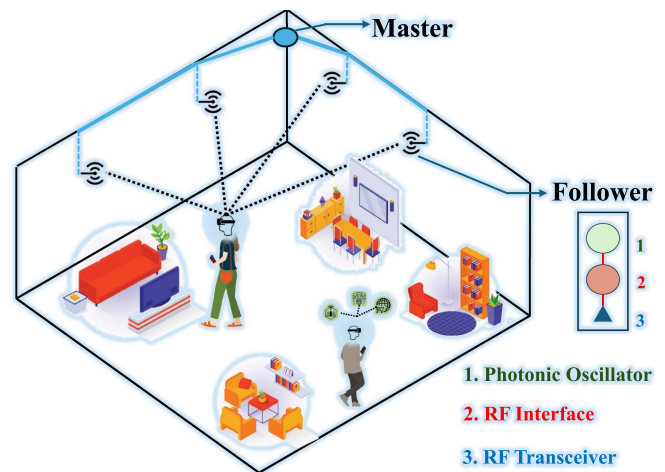


Fig. 1. General overview of the indoor positioning scenario using the IsoPos system, depicting a cluttered indoor environment with multiple moving users present.

A visual overview of the indoor positioning scenario within the IsoPos system is depicted in Fig. 1.

Furthermore, we demonstrate that the positioning error bound (PEB) of IsoPos is affected by ranging- and geometry-induced errors. Utilizing IPT and ILS mechanisms, IsoPos reduces the ranging-based errors substantially. The geometry-induced errors, on the other hand, are caused by the relative geometry between the positioning nodes and the user. Finding an optimal anchor placement that encompasses all possible user locations in a 3-D space is a known NP-hard problem [9]. To counter the adverse impact of relative geometry, we propose an optimization framework based on evolutionary algorithms (EAs). Our findings indicate that our proposed system leads to precise localization and tracking with sub-1 mm accuracy in all three dimensions, which is an order of magnitude improvement over existing systems that offer centimeter-level accuracy. These results demonstrate the potential of IsoPos as a highly accurate localization solution for real-world applications.

Our primary contributions are detailed as follows.

- 1) We present IsoPos, a high-accuracy 3-D localization system that uses the structure of photonic oscillators' isochrons and an injection locking scheme for precise timing and synchronization. IsoPos achieves a sub-tenth of a millimeter accuracy in distance estimation through the IPT protocol, which calculates ToA by measuring the induced phase shift in oscillations of the receiver, exploiting the intricate structure of its isochrons.
- 2) Utilizing the ILS protocol, IsoPos achieves precise synchronization among positioning nodes. This protocol leverages the tunable, robust limit cycles of injection-locked semiconductor lasers, enhancing the synchronization capabilities of photonic oscillators for improved localization accuracy.
- 3) We derive the PEB for IsoPos and attribute the positioning error to ranging- and geometry-induced errors. We design an optimization framework to address the NP-hard problem of mitigating geometry-induced errors.

- 4) Using commercially available semiconductor laser parameters, we design a comprehensive evaluation campaign to assess the performance of our proposed system. The numerical results confirm that IsoPos achieves sub-millimeter localization accuracy in three dimensions.

The rest of this article is organized as follows. Section II provides a concise overview of related work and background information relevant to our proposal. In Section III, we present the IsoPos overall framework and break down the system into three subblocks, providing a brief overview of each. Section IV is the core of this article, detailing the novel timing protocol used by IsoPos to measure ToA with extremely high resolution, which differs significantly from current state-of-the-art techniques. In Section VI, we demonstrate how high-resolution ToA measurements can be used to achieve high-accuracy 3-D positioning. We also derive the PEB of the system, highlighting that the accuracy is not solely based on the ToA measurement, but is also impacted by the relative geometry between the positioning nodes and the user. To address this issue, we propose an optimization framework in Section VII that determines better placements for the positioning nodes and mitigates geometry-induced errors. Section VIII presents our evaluation setup and final results. Finally, Section X concludes with a summary and discussion of ongoing research.

## II. RELATED WORK AND BACKGROUND

Our work is closely related to the following fields of study.

*Localization:* There exist three commonly used approaches to localization [19], [20], [21], namely, fingerprinting techniques [22], vision-based methods [23], and ranging-based schemes [24]. Localization methods based on fingerprinting that utilize received signal strength or channel state information are well-suited for coarse measurements but are susceptible to real-time fluctuations [25], [26], [27], [28]. Vision-based methods provide superior accuracy but are vulnerable in visually challenging environments (e.g., low-light conditions) [8]. Ranging-based solutions are reliable and can achieve precise localization even in dark areas. However, their accuracy is influenced by the quality of the received signal and the resolution of the system for time (ToA-based [29]) or angle (AoA-based [30]) measurements. High-resolution time measurements necessitate a broad bandwidth, which can restrict the system's operational range and deteriorate the quality of the signal propagation at higher frequencies due to the negative impact of channel characteristics. In order to improve the accuracy of existing ranging-based systems, we present a novel method for measuring ToA with high accuracy that is completely independent of the characteristic design (such as frequency and bandwidth) and the quality of the received RF signal. Our system does not require any demodulation or signal processing on the received RF signal, unlike conventional techniques. Instead, the RF signal is only used to initialize the system, and all measurements are based on the phase shifts induced in the photonic oscillators.

*Isochrons in photonic oscillators:* Receiver clocks can be effectively provided by photonic oscillators consisting of a set of coupled semiconductor lasers, owing to their exceptional

frequency tunability, compact design, and implementation in photonic integrated circuits [31], [32], [33]. A defining feature of a photonic oscillator is its ability to maintain self-sustained oscillations, representing a stable limit cycle inherent in the dynamical system that dictates its internal behavior. The oscillation frequency is uniquely determined by the system's parameters and encompasses a wide spectrum, extending from 100 MHz to well over 100 GHz [34], [35]. These oscillations are notably resilient when exposed to noise perturbations. They are distinctively defined by their frequency spectrum, as well as by their isochrons' structure. This structure plays a pivotal role in governing both their synchronization properties when subjected to periodic signals from an external controller and their phase shift in response to a user-emitted pulse that initiates the photonic oscillator.

The introduction of the concept of isochrons in oscillatory systems is attributed to Winfree [11] and has found extensive application within the realms of mathematical biology and neuroscience [13]. In a technological context, later studies of electronic oscillators have applied analogous concepts and methodologies, albeit using distinct terminologies and without explicit incorporation of the concept of isochrons [36], [37]. It is only recently that this concept has been applied to the examination of photonic oscillators, specifically concerning their synchronization dynamics and the formation of frequency combs [14], [15]. Famili et al. [38] introduced the concept of using isochrons for high-accuracy localization. However, their exploration was preliminary, lacking depth and failing to provide the PEB or insights into various error sources impacting localization accuracy. Their work was also deficient in thorough evaluation. In contrast, our study not only proposes the use of isochrons in nonlinear photonic oscillators for localization purposes but also delves deeply into the topic, presenting all the mathematical background of our derivations. We provide the PEB for our system and demonstrate how localization accuracy is influenced by both ranging-based and geometry-induced errors. Our approach addresses ranging-based errors with a novel time measurement and synchronization strategy, and offers an effective solution to mitigate the impact of spatial geometry on localization accuracy. To the best of the authors' knowledge, we are the first to comprehensively address this issue with an in-depth system evaluation.

*Optimal beacon placement:* The optimization of beacon placement for localization purposes in both indoor environments [39], [40], [41] and wireless networks [42], [43], [44], [45] has been extensively studied. The majority of the literature here primarily addresses two core challenges: first, ensuring comprehensive coverage by optimally determining both the quantity and locations of beacons [46], and second, refining beacon placement to minimize localization errors due to the spatial relationship between the user and positioning anchors [47]. In tackling the first challenge, the choice of sensor technology is crucial as it influences coverage capabilities. For instance, systems employing low-power Bluetooth sensors [48] benefit from omnidirectional transmission, although their effective range is constrained by physical barriers and distance. Conversely, systems utilizing ultrasound sensors must also consider the

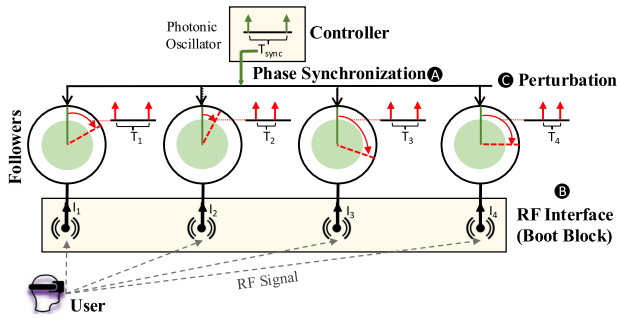


Fig. 2. System overview showing user connection to the RF interface of IsoPos to boot the follower oscillators by generating excitation pulses. Precise synchronization is achieved by periodic pulses generated through the controller oscillator passed to the followers through optical fiber links.

directional limitations imposed by the sensors' beam angles [49]. This aspect is particularly critical in complex structures, such as multistory buildings with multiple rooms, where determining an optimal number of beacons is vital. Beyond merely determining beacon quantity, the subsequent phase of optimization focuses on their strategic placement to mitigate errors introduced by the geometric configuration of beacons relative to the user, thereby enhancing localization accuracy [50].

In this work, a distinctive focus of our research lies in the optimal placement of a fixed number of beacons, assumed post the initial coverage optimization, to minimize the localization errors induced by the relative spatial geometry of the beacon arrangement. Unlike the prevailing research trends that concentrate primarily on mitigating ranging-based errors or identifying the minimum number of beacons necessary, our work delves deeply into the strategic positioning of beacons in addition to the mitigation strategies for ranging-based errors. To best of the authors' knowledge, this is the first approach that not only addresses ranging errors through newly proposed IPT and ILS protocols for enhanced timing measurements with high-resolution distance estimation and seamless synchronization but also rigorously focuses on optimizing beacon placement to reduce spatial geometry-induced errors. This approach enhances our system's capabilities in ranging-based localization, offering an integrated solution that significantly improves accuracy.

### III. SYSTEM MODEL

In this section, we provide a concise overview of the proposed localization approach, which is broken down into three functional blocks for clarity. In the following, we will elaborate on each block. The first two blocks mainly cover the IPT mechanism and timing procedure, while the third block covers the ILS protocol and synchronization. A schematic overview of the IsoPos mechanism is illustrated in Fig. 2.

*User RF transmission:* To initiate ToA measurement, we use the RF signal transmission between the user and the proposed system. This signal is denoted as  $s(t)$ . Due to the fact that the ToA measurement in our proposed approach does not require demodulation of  $s(t)$ , i.e., it is not based on the content of the received signal, we are able to design it freely and robustly

against environmental influences. Because the receiver knows  $s(t)$ , it ensures that only this signal can activate the system while rejecting all other signals. This design approach enhances system robustness against destructive environmental impacts.

*RF interface and follower oscillators:* The initial part of this block is the RF interface or booting block, which serves as an intermediary between our system and the physical world. It includes the control system for booting the follower oscillators, as depicted in Fig. 2. Upon the arrival of the designed  $s(t)$ , the RF interface's sole responsibility is to instantly boot the system. In other words, it causes the system to generate the necessary excitation pulses internally and feed them through optical fibers to the follower oscillators. The phase transition curve (PTC) quantifies the effect of an excitation pulse on each oscillator. Its shape is determined by the structure of the system's isochrons, and the induced phase shift can be used to determine the time instance at which the excitation pulse is generated. Since the booting block starts instantaneously after receiving the RF signal from the user, the measured time instance is the same as the ToA of the received RF signal. At the stage where the excitation pulses are fed into the follower oscillators, the amplitude of the excitation pulse can be set to be the same for all oscillators. It is noteworthy that this is independent of the received RF signal strength or quality, which can be different due to attenuation along different paths.

*Controller oscillator:* The last block of the system is the controller oscillator, which is in charge of synchronizing the phase of all the follower oscillators. This block leverages the combination of the injection-locking mechanism with the synchronization properties of the photonic oscillator under an externally modulated periodic signal. This allows precise synchronization among all follower oscillators and ensures that their initial phases are identical. As a result, all the phase shifts caused by the excitation pulses share a common frame of reference enabling the system to perform precise positioning based on time differences of arrivals. The stable phase-locking conditions for the amplitude and frequency of the external synchronizing signal are determined by the oscillator's isochrons' structure and corresponding phase response. Notably, synchronization of the follower oscillators is achieved by a periodic sequence of excitations modulating the injection rate of the controller oscillator, whereas for the measurement of ToA only, the effect of a single excitation pulse on each follower oscillator is required.

### IV. SYNCHRONIZATION PROTOCOL AND TIME-MEASUREMENT MECHANISM

Here, we present the ILS protocol used for synchronization and the IPT mechanism utilized for measuring ToA, which are the core contributions of IsoPos system and the foundations of our study. The following subsections delve into the essential preliminaries and in-depth approach details concerning *photonic oscillators*, *isochrons*, and *time measurement* concepts.

#### A. Photonic Oscillator Model

A fundamental tunable photonic oscillator consists of two coupled semiconductor lasers in a controller-follower

configuration, where the output of the former is optically injected into the latter. The semiclassical description of this system is given by the following set of differential equations for the complex amplitude  $E$  of the optical field ( $E_{\text{opt}}(\tau) = E(\tau)e^{i\omega_0\tau}$ ) and the carrier density  $n$ :

$$\begin{aligned}\frac{dE}{d\tau} &= \frac{\Gamma G_N}{2}(1 + i\alpha)nE + \kappa E_{\text{in}}e^{i\nu\tau} \\ \frac{dn}{d\tau} &= \frac{J - J_{\text{th}}}{e} - \frac{n}{\tau_s} - \left(\frac{1}{\Gamma\tau_p} + G_N n\right)|E|^2\end{aligned}\quad (1)$$

where the optical field has been renormalized such that the power  $|E|^2$  represents the number of photons in the active layer, the injected monochromatic optical field is  $\mathcal{E}_{\text{in}}(\tau) = E_{\text{in}}(\tau)e^{i\omega_{\text{in}}\tau}$ , and  $\tau$  denotes real time. The parameter  $\Gamma$  is the confinement factor,  $\alpha$  is the linewidth enhancement factor,  $J$  is the pump current, whereas  $J_{\text{th}}$  is the threshold current,  $e$  is the elementary charge,  $\tau_p$  and  $\tau_s$  are the photon and carrier lifetimes, respectively—typically measured in psec—and  $G_N$  is the gain coefficient at transparency. The parameters  $\kappa$  and  $\nu$  correspond to the injected field and denote the injection rate and the detuning between the injected signal and the follower laser, respectively. By introducing the new time  $t$  and the new dependent variables  $x, y, Z$

$$\begin{aligned}t &\equiv \frac{\tau}{\tau_p}, \quad x \equiv \text{Re}\left(\sqrt{\frac{\tau_s G_N}{2}}E\right) \\ y &\equiv \text{Im}\left(\sqrt{\frac{\tau_s G_N}{2}}E\right), \quad Z \equiv \frac{\Gamma G_N \tau_p}{2}n\end{aligned}\quad (2)$$

a set of dimensionless nonlinear differential equations for the normalized complex electric field  $\tilde{E} = x + iy$  and the normalized excess carrier density  $Z$  can be obtained

$$\begin{aligned}\frac{dx}{dt} &= (x - \alpha y)Z + \Omega y + \eta \\ \frac{dy}{dt} &= (y + \alpha x)Z - \Omega x \\ T\frac{dZ}{dt} &= P - Z - (1 + 2Z)(x^2 + y^2)\end{aligned}\quad (3)$$

where

$$\begin{aligned}T &\equiv \frac{\tau_s}{\tau_p}, \quad P \equiv \frac{\tau_s \tau_p G_N \Gamma}{2} \left(\frac{J - J_{\text{th}}}{e}\right) \\ \eta &\equiv \sqrt{\frac{\tau_s G_N}{2}} \tau_p \kappa E_{\text{in}}, \quad \Omega \equiv \nu \tau_p.\end{aligned}\quad (4)$$

$T$  is the ratio of carrier to photon lifetimes,  $P$  is the normalized excess electrical pumping rate of the follower laser,  $\eta$  the normalized injection rate, and  $\Omega$  the normalized detuning between the frequency of the controller laser and the frequency of the free-running follower laser [51].

As a nonlinear system, this setup is known to have a rich set of dynamical features ranging from stable steady states, and limit cycles born out of Hopf bifurcations, to chaotic outputs [52]. For our purpose, we focus on the well-defined parameter range where this system supports stable limit cycles

TABLE I  
PARAMETER VALUES FOR A SEMICONDUCTOR LASER [52]

linewidth enhancement factor	2.6
Carrier lifetime	250 ps
Photon lifetime	2 ps
Detuning	5 GHz
Injection	0 – 0.0743
Period of limit cycle	0.2 – 0.08 ns

corresponding to self-sustained oscillations. Each limit cycle is characterized by its period  $T_{\text{lc}}$  (in the following analysis,  $T_{\text{lc}}$  has been renormalized to 1), its spectral content (discrete spectral lines at integer multiples of  $f_{\text{lc}} = T_{\text{lc}}^{-1}$ , since it is in general nonharmonic) and by the rate of convergence of nearby initial conditions toward the limit cycle. Moreover, the limit cycle is characterized by a phase variable parameterizing each point of the cycle, as represented in Fig. 3(a). The concept of the phase can also be extended outside the limit cycle by introducing the asymptotic phase function [11], which is defined as the relative phase with which an initial condition ends up in the limit cycle. Isochrons are defined as the locus of the initial conditions, within the basin of attraction of the limit cycle, that have the same asymptotic phase [11], and partition the phase space, as shown in Fig. 3(b) and (c). The structure of the isochrons determines the phase response [12] of the limit cycle to a pulse kick of amplitude  $A$  that moves the system to an initial condition outside the limit cycle, as illustrated in Fig. 3(c). The relation between the phase of the oscillation at the time when the pulse arrives and the new (asymptotic) phase is provided by the PTC

$$\text{PTC}(\theta) = \theta_{\text{new}} \bmod 1 \quad (5)$$

or the phase response curve (PRC)

$$\text{PRC}(\theta) = \theta_{\text{new}} - \theta. \quad (6)$$

Depending on the amplitude of the kick, the PTC can be either invertible (Type 1) or noninvertible (Type 0), as shown in Fig. 4. For the realistic values exhibited in Table I, the laser exhibits a stable intensity oscillation, characterized by the presence of a periodic orbit that exhibits a decreasing period in response to an increase in the injection strength. As an example, we select a moderate injection strength  $\eta = 0.04$  that corresponds to  $T_{\text{lc}} \simeq 0.1$  ns.

The isochrons of the system are computed as level sets of the time average of an observable  $f$  along the trajectories of the system [53]

$$f_{i\omega}^* = \lim_{T \rightarrow \infty} \frac{1}{T} \int_0^T f \circ \phi^\tau(x, y, Z) e^{-i\omega\tau} d\tau \quad (7)$$

where  $\omega$  represents the dimensionless angular frequency of the limit cycle,  $f = x^2 + y^2 \equiv I$ , i.e., the dimensionless intensity of system (3), and  $\phi: \mathbb{R}^+ \times \mathbb{R}^3 \rightarrow \mathbb{R}^3$ , i.e.,  $\phi(t, x, y, Z) = \phi^t(x, y, Z)$ , is the flow describing the dynamics of (3). This integral is evaluated numerically over a finite time horizon,  $\bar{T} = kT_{\text{lc}}$ ,  $k \in \mathbb{Z}$ . Longer time horizons lead to better convergence toward the limit cycle, resulting in a more accurate calculation of the asymptotic phase.

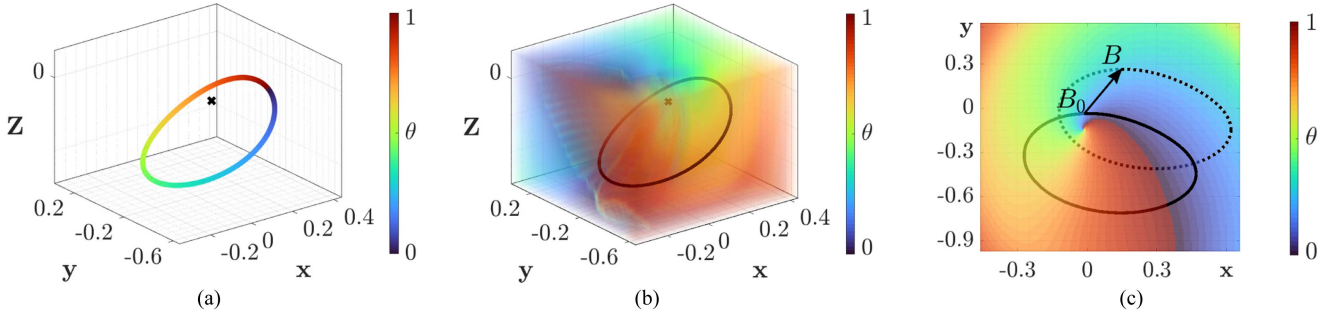


Fig. 3. (a) Definition of phase function  $\theta$ —measured in units of  $T_{lc}$ —on the limit cycle. The closed curve corresponds to the limit cycle, while the black  $\times$  point corresponds to one unstable equilibrium of the system. (b) Isochrons' structure in the phase space of the system. (c) Asymptotic phase on the section  $Z = 0$  of the phase space. The closed continuous curve corresponds to the projection of the limit cycle of the system on this section, while the closed dashed curve corresponds to the projection of the perturbed initial conditions on this section.  $B_0$ : Point on the limit cycle, and  $B$ : Perturbed initial point of the system.

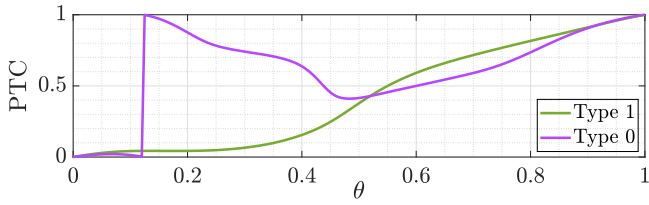


Fig. 4. PTC. Type 1 PTC: Invertible; small-amplitude excitation. Type 0 PTC: Noninvertible; large-amplitude excitation.

### B. Follower Oscillators Synchronization

IsoPos employs the TDoA technique to address the lack of synchronization that arises between the user and the localization system. As such, it is imperative to establish perfect synchronization among the anchors in the localization system. However, achieving perfect synchronization remains a significant challenge in the current state of the art, as even minute deviations can have a substantial impact on the overall accuracy of the system. To that end, we propose the ILS mechanism that uses the controller–follower phase-lock injection scheme. Based on that, the injected power is modulated with a synchronization signal consisting of a train of periodic pulsatile stimulations of magnitude  $A$  delivered with a period  $T_s$  (in units of  $T_{lc}$ )

$$\eta(t) \rightarrow \eta + A \sum_{n=1}^m \delta(t - nT_s). \quad (8)$$

The phase  $\theta_{n+1} \in [0, 1)$  at the moment of every stimulus ( $n + 1$ ) is

$$\theta_{n+1} = [PTC(\theta_n, A) + T_s] \bmod 1 \quad (9)$$

where  $\theta_n$  is the phase of the system before the stimulus. This equation defines a Poincaré mapping of the interval  $[0, 1)$  to itself, i.e., a circle map that governs the synchronization dynamics of the driven system. The fixed points  $\theta^*$  of this mapping correspond to phase locking and are given by the following equation:

$$PRC(\theta^*) = 1 - T_s \quad (10)$$

expressing that synchronization is achieved when the stimulated phase kick compensates for the frequency detuning between

the periods of the limit cycle and the synchronization signal. The stability condition of the fixed point, and therefore the synchronization process, is determined by the slope of the PRC as follows:

$$-2 < PRC'(\theta^*) < 0. \quad (11)$$

The stability of the fixed point is related to the robustness of the synchronization process under the presence of noise and/or small parameter deviations. The slope value  $\mu = PRC'(\theta^*) = PTC'(\theta^*) - 1$  is equivalent to the characteristic multiplier governing the convergence of nearby initial conditions to the fixed point. Synchronization dynamics of the Poincaré mapping toward a fixed point corresponding to a phase-locked state are depicted in Fig. 5. Given the parameter values specified in Table I, it is possible to achieve synchronization among the four follower oscillators, having different (random) initial phases, through a sequence of 30 pulsatile stimulations of amplitude  $A = 0.35$  delivered every 1.105 ns. It is worth mentioning that the above analysis ensures that the system evolves to the desired phase-synchronized periodic state, which is appropriate for its function as a clock, and not to chaotic states existing outside the domain of the above stability conditions [14], [15].

### C. Fine Time Measurements

Here, we outline the IPT mechanism to demonstrate how the ToA measurements work in IsoPos. With each follower oscillator phase-synchronized using ILS protocol under the action of the controller synchronization signal, a pulse is received from the boot block at a different ToA in each oscillator, depending on its distance from the user. This signal pulse arrives when the oscillator's cycle is at a specific phase  $\theta_{in}$  and kicks the oscillator to a new phase  $\theta_{out}$ , with the two phases related through the PTC. The new phase  $\theta_{out}$  can be readily exploited for determining the phase upon pulse arrival  $\theta_{in}$  when the PTC is invertible (Type 1), as in Fig. 4, and in regions where multistability [15] does not take place, namely, for relatively small pulse amplitudes. This condition dictates the common amplitude of the pulse that is fed to the follower oscillators from the boot block. The ToA of the user signal in each oscillator is calculated from the  $\theta_{in}$  with the PTC given as a lookup table. Based on the application, either

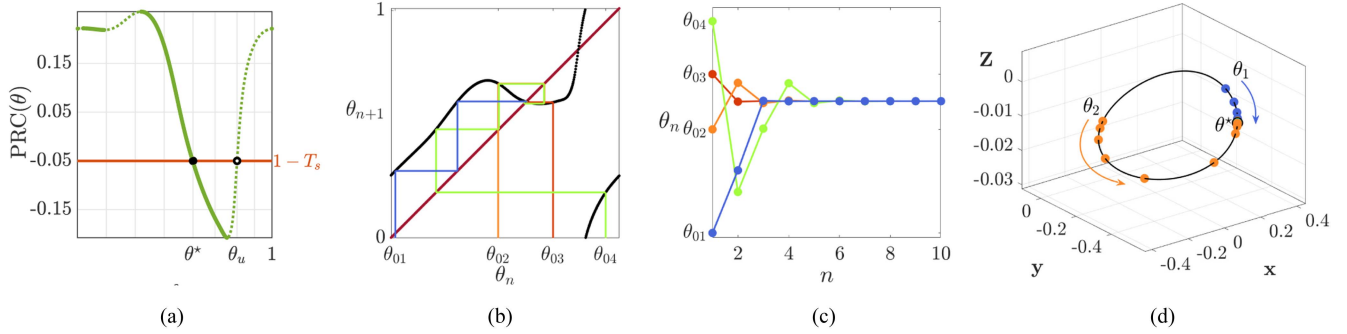


Fig. 5. (a) PRC corresponding to a stimulation of amplitude  $A = 0.35$  of the limit cycle in Fig. 3(a). The continuous part of the PRC indicates the region of existence of stable fixed points, i.e., (11) is satisfied. (b) Cobweb diagram for the evolution of the four initial conditions to a stable fixed point of the circle map (9). (c) and (d) Convergence of  $\theta_n$  – orbits with varying initial conditions to a stable fixed point of (9), meaning that phase locking is achieved.

this time is in the same cycle that we know or a number of cycles have to be added to it based on the coarse measurement.

#### D. Time Scales and Accuracy

Resolution and accuracy in phase and time measurements depend on three characteristics: 1) the frequency of the limit cycle  $f_{lc}$ , 2) the convergence rate towards the stable limit cycle, and 3) the slope  $\mu$  of the PRC at the fixed point.

The frequency  $f_{lc}$  determines the coarse time unit, whereas the final time and, consequently, the localization resolution is determined by the division of the oscillation cycle into a discrete set of isochrons. Since there are no inherent restrictions on the level of discretization of the continuous isochrons' structure, an exceptionally high resolution can be achieved without resorting to extremely high frequencies that would raise technological requirements. The convergence rate toward the limit cycle dictates the time required for the system to return to the oscillation with the new asymptotic phase after receiving a user signal. This rate indicates the limit cycle's robustness and imposes a restriction on the update speed for user positioning. The slope  $\mu$  provides a measure of the convergence speed of the synchronization process for the follower oscillators. It is notable that the remarkable tunability of the optically injected system allows for appropriate parameter selections in order to have sufficiently large frequencies  $f_{lc}$  ranging from 100 MHz to larger than 100 GHz [34], [35] as well as desired convergence rates for negligibly small waiting times, at the order of nanoseconds (ns), and sufficiently high update rates for user positioning, even when moving with a high speed.

#### V. NOISE ANALYSIS

The 1-D discrete Poincaré phase map is sufficient for examining the synchronization properties of our photonic oscillators. Given the inevitability of noise in any real system, a sensitivity analysis of (9) for the effect of noise on the synchronization of the different nodes, according to the ILS approach, facilitates a comprehensive understanding of the system's resilience to noise sources.

The synchronization dynamics, for a specific set of parameter values, under ideal conditions is described in Section IV-B. For

the noise analysis, the amplitude of the external modulation is considered as the deterministic component of our system, whereas the period of the external modulation is considered as the stochastic one. This simplification is justified by the significantly larger difficulty in frequency and phase stabilization in comparison to amplitude stabilization in the production of periodic waveforms, in general. For a periodic pulse sequence, an amplitude equalizer can ensure amplitude stability, whereas the requirement for a constant time spacing between subsequent pulses is more difficult to be achieved.

The period of the external controller signal is considered as a stochastic component by introducing white noise into (9), where the modified  $T_s$  is expressed as  $T_s + \xi(n)$ ;  $\xi(n)$  represents the additive white noise of density  $D \equiv \tilde{\sigma}^2/2$  applied to  $T_s$  at time step  $n$ , sampled from a Gaussian probability distribution with mean value  $\tilde{\mu} = 1.05$  and standard deviation  $\tilde{\sigma}$ , as in Fig. 6(a).

To assess the robustness of the desired phase-synchronized periodic state, which is necessary for having the same time bias in all nodes, we consider a progressive increment in white noise density and study the distribution of the final phase of the periodic state. For each specific value of the noise density,  $L$  realizations of discrete phase orbits of length  $N$  are generated using the iterative process described by (9) with the modified  $T_s$ . The first half of each orbit is discarded to eliminate transient effects and its corresponding variance  $\sigma_\theta^2$  is calculated. For low noise density levels,  $\theta_n$ –orbits also follow a Gaussian probability distribution with mean value close to  $\theta^*$  and standard deviation  $\sigma_\theta$ ; see Fig. 6(b). Upon averaging the mean variance across all realizations and examining its response to increasing noise levels, one can deduce that the noise present in the Poincaré phase map does not undergo amplification, as seen in Fig. 7.

#### VI. 3-D POSITIONING

First, Section VI-A introduces the 3-D localization method used by IsoPos. Following that, in Section VI-B, the PEB of the proposed scheme is derived.

##### A. Trilateration Localization

Following the successful measurement of the ToA at each of the follower oscillators, which is based on their phase response

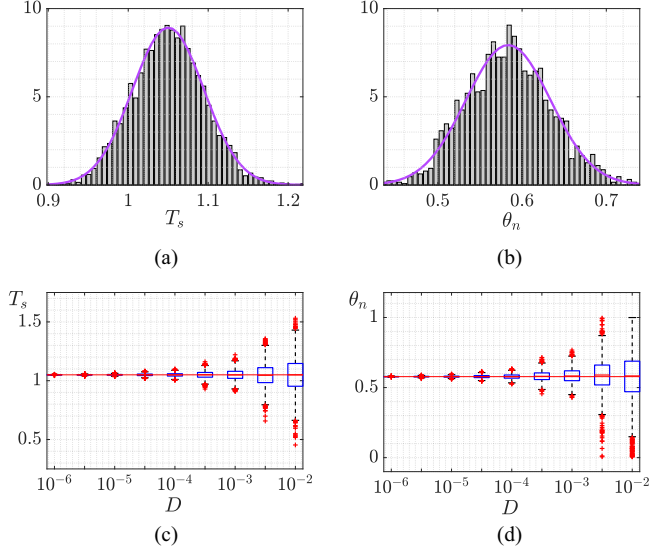


Fig. 6. Bar graphs representing (a)  $T_s$  and (b)  $\theta_n$  values for a single realization and noise density  $D = 10^{-3}$ . Magenta curves depict the corresponding normal distributions. Box plots representing (c)  $T_s$  and (d)  $\theta_n$  values across increasing noise density levels for a single realization. Within each plot, the box's lower and upper boundaries denote the 25th and 75th percentiles, respectively. The vertical span of the box signifies the interquartile range (IQR). Dashed lines extending from the box represent whiskers, with a length of 1.5 times the IQR. The red line segments within the box denote the sample median, whereas outliers (red symbols) correspond to values exceeding 1.5 times the IQR. Red lines correspond to (c)  $T_s = \bar{\mu}$  and (d)  $\theta_n = \theta^*$ .

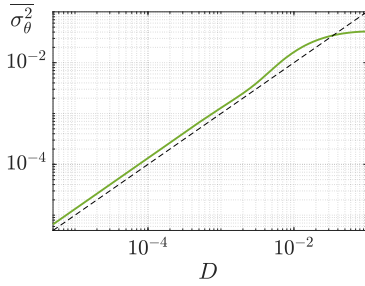


Fig. 7. Average of  $\sigma_\theta^2$  over  $L = 1000$  realizations of  $\theta_n$ -orbits of length  $N = 2^{12}$  as noise density increases (continuous line); bisector of the first quadrant angle (dashed line).

to the periodic impulse excitation signal, the user's final location in 3-D space is determined. To accomplish this, the times must be converted to distances and the distances must be trilaterated.

The RF signal transmitted by the target user and the localization system (i.e., the follower oscillators) are not synchronized. However, due to the controller injection-locking procedure, all of the follower oscillators have synchronized phases, implying that all of the measured ToAs in different follower oscillators have a synchronized clock. This means that all of the received times have the same synchronization bias, and the distances between the user and follower oscillators can be written as follows:

$$r_i = c \times (t_i - t_T + \beta) = c \times (\tau_i + \beta) \quad (12)$$

where  $r_i$  represents the corresponding distance between the user and the  $i$ th follower oscillator,  $t_i$  is the received time at the  $i$ th

follower oscillator,  $t_T$  is the transmit time, i.e., the time that the signal left the RF transmitter on the user,  $\beta$  is the synchronization bias between the transmitter clock on the user and any of the follower oscillators,  $\tau_i$  is the propagation time delay between the RF transmitter on the user and the  $i$ th receiver follower oscillator, and  $c$  is the speed of light;  $i \in \{0, \dots, N-1\}$ , where  $N$  is the number of follower oscillators, which equals four in our design. For 3-D localization, the minimum number of four positioning nodes is required.

The actual distances are unknown due to the  $\beta$  synchronization bias between the transmitter and each of the receivers, as shown in (12). However,  $\beta$  can be eliminated if we take one of the follower oscillators as the reference and subtract the rest from it as shown in the following:

$$r_i - r_0 = c \times (t_i - t_0) \quad (13)$$

where  $i \in \{1, \dots, N-1\}$ , and the precise measurement of  $t_0$  and all the remaining  $t_i$  values are available. A hyperboloid is the geometrical representation of a set of points in 3-D space with a constant distance subtraction to known points (the foci). The user's 3-D location is represented by the intersection of all these hyperboloids. The mathematical model for finding the intersection is as follows:

$$[x \ y \ z]^T = \min e(x, y, z) \quad (14)$$

where  $[x \ y \ z]^T$  is the location of the user in a Cartesian coordinate system and  $e(x, y, z)$  is defined as

$$e(x, y, z) =$$

$$\sum_{i=1}^{N-1} \left\{ (r_i - r_0) - \sqrt{(x_i - x_0)^2 + (y_i - y_0)^2 + (z_i - z_0)^2} \right\}$$

where  $[x_i \ y_i \ z_i]^T$  values are the Cartesian coordinates of the  $i$ th receiver follower oscillator.

## B. Positioning Error Bound

In this section, we calculate the PEB for the proposed localization system. As previously stated, an accurate estimate of  $r_i$  is not available. However, the precise clock synchronization among the positioning system's follower oscillators, achieved through injection phase-locking, enables the difference  $r_i - r_j$  to be computed with high accuracy. The reference oscillator is  $r_0$  for the remainder of the process, and the  $r_i - r_0$  values are calculated as follows:

$$r_i - r_0 = \sqrt{(x - x_i)^2 + (y - y_i)^2 + (z - z_i)^2} - \sqrt{(x - x_0)^2 + (y - y_0)^2 + (z - z_0)^2}. \quad (15)$$

Because of the ranging measurement errors, the precise  $r_i - r_0$  is unknown, resulting in errors when solving for  $[x \ y \ z]^T$  in (15). The variance of the 3-D location estimator is required to find a correlation between the overall 3-D location error,  $\sigma_T(x, y, z)$ , and the distance estimation ranging errors,  $\sigma_{r_i}$ , that come from the measurement devices

$$\sigma_T(x, y, z) = \sqrt{\sigma_x^2 + \sigma_y^2 + \sigma_z^2} \quad (16)$$



where  $(\sigma_x^2, \sigma_y^2, \sigma_z^2)$  are the variances of the error for  $x$ -,  $y$ -, and  $z$ -axes estimation, respectively. Let  $\Delta\mathbf{X} = [\Delta x \ \Delta y \ \Delta z]^T$  be the derivative on the overall  $[x \ y \ z]^T$  estimations; then, we have

$$\text{Cov}(\Delta\mathbf{X}) = \mathbf{E}(\Delta\mathbf{X}\Delta\mathbf{X}^T) = \begin{bmatrix} \sigma_x^2 & \sigma_{xy} & \sigma_{xz} \\ \sigma_{yx} & \sigma_y^2 & \sigma_{yz} \\ \sigma_{zx} & \sigma_{zy} & \sigma_z^2 \end{bmatrix}. \quad (17)$$

As a result, for the variance of the overall location estimation, based on (16), we have

$$\sigma_T^2(x, y, z) = \text{Trace}(\mathbf{E}(\Delta\mathbf{X}\Delta\mathbf{X}^T)) \quad (18)$$

and  $\text{Trace}(\cdot)$  denotes the sum of the diagonal elements of the matrix. Then, the correlation between  $\sigma_T^2(x, y, z)$  and the  $\sigma_{r_i}^2$  is calculated. For this, we differentiate (15), that is

$$\begin{aligned} \Delta r_i - \Delta r_0 &= \frac{\Delta x(x - x_i) + \Delta y(y - y_i) + \Delta z(z - z_i)}{\sqrt{(x - x_i)^2 + (y - y_i)^2 + (z - z_i)^2}} \\ &\quad - \frac{\Delta x(x - x_0) + \Delta y(y - y_0) + \Delta z(z - z_0)}{\sqrt{(x - x_0)^2 + (y - y_0)^2 + (z - z_0)^2}} \end{aligned} \quad (19)$$

where second-order and higher order terms have been neglected. For the localization system with  $N$  follower oscillators, (19) can be written as  $\Delta\mathbf{R}_i - \Delta\mathbf{R}_0 = \Psi\Delta\mathbf{X}$ , or equivalently  $\Delta\mathbf{X} = (\Psi^T\Psi)^{-1}\Psi^T(\Delta\mathbf{R}_i - \Delta\mathbf{R}_0)$ , where  $\Delta\mathbf{R}_i = [\Delta r_1 \ \cdots \ \Delta r_{N-1}]^T$ ,  $\Delta\mathbf{R}_0 = [\Delta r_0 \ \cdots \ \Delta r_0]^T$ , and

$$\Psi = \begin{bmatrix} \frac{x-x_1}{r_1} - \frac{x-x_0}{r_0} & \frac{y-y_1}{r_1} - \frac{y-y_0}{r_0} & \frac{z-z_1}{r_1} - \frac{z-z_0}{r_0} \\ \vdots & \vdots & \vdots \\ \frac{x-x_{N-1}}{r_{N-1}} - \frac{x-x_0}{r_0} & \frac{y-y_{N-1}}{r_{N-1}} - \frac{y-y_0}{r_0} & \frac{z-z_{N-1}}{r_{N-1}} - \frac{z-z_0}{r_0} \end{bmatrix}.$$

Without loss of generality, we can assume  $\text{Var}(r_i) = \sigma_r^2$  and the errors  $\Delta r_i$  to be uncorrelated; therefore, we have

$$\begin{aligned} \text{Cov}(\Delta\mathbf{X}) &= ((\Psi^T\Psi)^{-1}\Psi^T)(\mathbb{I}_{N-1} + \mathbb{J}_{N-1})((\Psi^T\Psi)^{-1}\Psi^T)^T \sigma_r^2 \end{aligned}$$

where  $\mathbb{I}_{N-1}$  is the identity matrix of size  $(N-1) \times (N-1)$  and  $\mathbb{J}_{N-1}$  is the  $(N-1) \times (N-1)$  matrix with all its entries equal to one. It is important to emphasize that in the IsoPos system, we assume  $\text{Var}(r_i) = \sigma_{r_i}^2 = \sigma_r^2$ , indicating that all receivers share the same error variance in distance estimation. This assumption may not entirely reflect reality, as different receivers might exhibit variations in error due to multiple factors. However, for the purpose of deriving the closed-form PEB for IsoPos, we consolidate these variances by adopting the largest value as the common error variance for all receivers. This conservative approach ensures that without compromising the generality of the problem, we account for the worst-case scenario by considering the highest  $\sigma_{r_i}^2$  as the uniform error variance for all receivers, allowing us to proceed with our analysis. Based on (18), the variance of the 3-D location estimator is given by

$$\sigma_T^2(x, y, z) = G(x, y, z) \cdot \sigma_r^2 \quad (20)$$

where  $G(x, y, z)$  is defined as

$$\text{Trace}(\Phi(\mathbb{I}_{N-1} + \mathbb{J}_{N-1})\Phi^T); \quad \Phi = (\Psi^T\Psi)^{-1}\Psi^T. \quad (21)$$

As a result, two factors influence overall location accuracy: 1) the geometry-induced error  $G(x, y, z)$ , which is primarily tied to the relative geometry between the elements of the localization system and the user; and 2) the ranging-error  $\sigma_r^2$ , which is caused by ranging measurements errors.

## VII. OPTIMAL PLACEMENT OF FOLLOWER OSCILLATORS

The previous section illustrated that accurate 3-D user localization cannot be achieved only with precise time and distance estimation. To attain high-accuracy 3-D localization, the configuration of the localization system components is also essential.

The primary goal of current state-of-the-art research is to reduce ranging-induced errors while ignoring the geometry-induced source [24], [27], [54]. Even though advanced commercial geolocation systems take this into account when making calculations, their effects still cannot be completely eliminated. This is because it is inherently difficult to determine the ideal anchor placement in 3-D space for a moving user in order to minimize geometric-induced errors at all points [55]. This is an NP-hard open problem [47].

In addition,  $G(x, y)$  is typically not excessively dependent upon various deployments. The majority of the available literature studies 2-D localization. Therefore, since the users do not move along the  $Z$ -axis, the negative effect of geometry is not obvious in their final solutions. Nevertheless, based on our experiments,  $G(z)$  is significantly more sensitive to the deployment of positioning nodes, and a random placement may result in a very high  $G(z)$ , resulting in an unreliable height estimation.

We present an optimization algorithm for determining the optimal deployment of follower oscillators for any given floor plan in order to alleviate the geometry-induced localization error. By constraining average  $G(x, y)$  and  $G(z)$ , the proposed algorithm improves estimation accuracy on the  $X - Y$  plane (horizontal) and  $Z$ -axis (vertical), respectively. We made use of two constraints on  $G(x, y)$  and  $G(z)$  in order to reach a solution to the NP-hard problem in a timely manner. Once these two constraints are satisfied, the placement configuration with the smallest  $G(x, y, z)$  value represents the ultimate solution. Although there may be other solutions with similar or lower values of  $G(x, y, z)$ , our primary objective is to guarantee that the relative geometry of the anchor placement does not significantly impact the location estimation for any point in the room. As a result, finding a placement that meets the desired thresholds for  $G(x, y)$  and  $G(z)$  satisfies our ultimate objective. This subtle but significant factor accelerates our optimization algorithm while preserving our objective of minimizing the effect of geometry on the overall location estimation of all points in the space.

In the rest of this section, we explain the details of our proposed optimization framework. In Section VII-A, we formulate the NP-hard optimal placement problem followed by the illustration of the optimization algorithm's mechanism in Section VII-B.

**Algorithm 1:** Follower Oscillators Deployment Algorithm.

---

**Input:** User domain ( $\mathbb{U}$ ), Anchor domain ( $\mathbb{A}$ ),  $\overline{G(x, y)}$  threshold ( $h_T$ ),  $\overline{G(z)}$  threshold ( $v_T$ )

**Output:** Desirable placement for a set of four follower oscillators

- 1: **while**  $\overline{G(z)} > v_T$  &  $\overline{G(x, y)} > h_T$  **do**
- 2:   Generate a set of  $P_T$  random individuals, where each individual is a set of four follower oscillator anchors
- 3:   **for**  $i = 1$  to  $i = \text{number of iteration}$  **do**
- 4:     Check the fitness of all available individuals;
- 5:     Kill the worst ones to keep having  $P_T$  individuals;
- 6:     Select the individuals with better fitness as parents;
- 7:     Crossover every two adjacent parents, make an offspring;
- 8:   **end for**
- 9: **end while**

---

### A. Problem Formulation

Given the user's constant mobility, it is insufficient to compute  $G(x, y, z)$ ,  $G(x)$ , and  $G(z)$  for a single position. As a result, we calculated the average of the  $G(x, y, z)$ ,  $G(x, y)$ , and  $G(z)$  for all possible indoor locations based on the provided floor plan.

Our primary goal is to determine the optimal placement for a set of four follower oscillators by minimizing the average of  $G(x, y, z)$  while keeping the averages of  $G(x)$  and  $G(z)$  below the required thresholds. The concluding optimization framework can be expressed as follows:

$$\begin{aligned} \min \quad & \sum_{\mathbb{U}} \text{Trace}(\Phi(\mathbb{I}_{N-1} + \mathbb{J}_{N-1})\Phi^T) \\ \text{s.t.} \quad & \overline{G(x, y)} < h_T; \overline{G(z)} < v_T \end{aligned}$$

where  $\mathbb{U}$  is the user domain, which is a subspace of the indoor environment including all the possible user positions,  $\Phi$  comes from (21),  $h_T$  and  $v_T$  are the threshold values for  $\overline{G(x, y)}$  and  $\overline{G(z)}$ , respectively;  $\overline{G}$  represents the average of  $G$ .

Our primary objective is to minimize  $\overline{G(x, y, z)}$  to determine the optimized anchor placement for mitigating the negative impact of relative geometry and improving localization accuracy. In the meantime, to maintain low horizontal and vertical estimation errors, we enforce the constraints for  $\overline{G(x, y)}$  and  $\overline{G(z)}$ , respectively. This ensures that enhancing the overall localization accuracy is done by improving both the  $X - Y$  plane estimation and  $Z$ -axis estimation. Optimization calculations are conducted over all the points in  $\mathbb{U}$ .

The positioning system nodes (i.e., the follower oscillators) may be located anywhere within the anchor domain, denoted by set  $\mathbb{A}$ . This includes the entire ceiling as well as the top portion of each side wall.

### B. Optimization Framework

We construct Algorithm 1 that is based on the EAs class [56] to find a solution with the least amount of computation time.

In our EA setup, an initial set of  $P_T$  random individuals is first produced. Four follower oscillators, chosen at random from the

domain  $\mathbb{A}$ , make up each individual. We divide the individuals into various groups to prevent getting caught in local minima.

Following generation, the individuals are sorted according to the fitness (cost) function and selected for reproduction based on the outcome. The fitness function is the  $\overline{G(x, y, z)}$  over the entire set  $\mathbb{U}$  obtained by arranging four follower oscillators in a specific manner. The algorithm then selects the first  $P_s$  individuals to serve as a parent group for the reproduction of new individuals. Using a crossover technique, every two adjacent pairs create a new set of four follower oscillators, resulting in a total of  $P_s/2$  offspring. The algorithm then checks the fitness function of each new individual once more. The last  $P_k = P_s/2$  in terms of fitness are eliminated from the total population of  $P_n = P_T + P_s/2$ , including both parents and offspring, leaving  $P_T$  as the number of the final individuals at the end of each stage.

Each set of parents includes eight follower oscillators in total, four per parent, for generating new offspring. The crossover technique replaces the first four follower oscillators' coordinate parameters with those from the second set.

We repeat the process for  $N_{\text{iter}}$  iterations. Following the completion of the iterations, the first individual in the line according to the fitness function is chosen. If it has  $\overline{G(x, y)}$  and  $\overline{G(z)}$  over the entire set  $\mathbb{U}$  that is less than  $h_T$  and  $v_T$ , respectively, it represents the final solution as the four follower oscillator placement configuration. Otherwise, the algorithm restarts the procedure by generating a new set of  $P_T$  individuals. When the final result satisfies the constraints, the algorithm terminates.

The parameters  $P_T$ ,  $P_s$ , and  $N_{\text{iter}}$  are established during the preprocessing stage, considering the provided floor plan. It is essential to underscore that our primary contribution does not revolve around the proposal of this algorithm to mitigate geometry-induced errors. Rather, this part serves as a complementary element aimed at enhancing the overall system's performance by reducing second error sources. The main thrust of our work resides in the introduction of innovative timing and synchronization mechanisms, as expounded upon in preceding sections. Consequently, allocating additional time for the assessment of the optimality or comparative analysis with an alternative optimization algorithm is deemed unnecessary within the scope of this study.

## VIII. PERFORMANCE EVALUATION

This section includes an assessment of the optimal anchor placement algorithm in Section VIII-A, followed by a comprehensive evaluation of the entire IsoPos system in Section VIII-B.

To provide a comprehensive assessment, we have established an extensive simulation campaign using *MATLAB R2022b*, running on a *Dell Optiplex 7080* computer equipped with an Intel i9 CPU and 64 GB of RAM. For the benchmark simulations, we locate the positioning nodes (i.e., the follower oscillators) within the room where user localization is required, keeping them spatially separated to avoid taking up valuable space or interfering with other objects in the environment. Regardless of the room's shape or dimensions, we suggest installing the positioning system nodes on the ceiling, thus preserving room aesthetics and functionality while the user can move freely to any point within the room. Also, we consider every possible

location for the user within the room. At each location, we know the exact position of the user, which serves as the ground truth. The user's location for each specific spot is then estimated using our proposed system, and the discrepancy between the ground truth and the estimated location constitutes the localization error. We utilize a Rician channel model to simulate the multipath effects and also add Additive White Gaussian Noise to all our simulations to mimic the typical indoor setup's multipath and noise characteristics.

To ensure a comprehensive evaluation and to account for various scenarios, our analysis also includes the movement of the user and, importantly, the presence of other individuals in the environment and their effect on performance evaluation. The scenarios are categorized as follows.

- 1) *User movement*: The system's performance is evaluated at every conceivable point a user might traverse. This includes lateral movements across various directions on the ground as well as vertical motions such as sitting, standing, and circumambulating.
- 2) *Movement of others*: The performance implications of other individuals moving within the vicinity of the user are critically assessed. Particularly, the impact on the line-of-sight (LoS) signal between the user and the positioning system is examined. Should the LoS be entirely obstructed, real-time localization ceases momentarily, defaulting to the last confirmed position. This fallback can result in minor positional discrepancies if the user continues to move, although it remains precise if the user is stationary. Furthermore, nonobstructive interference from nearby users may degrade the communication link, introducing additional errors. In contrast, movements occurring at a considerable distance from the user generally do not impact the system performance. All such scenarios have been simulated, with errors appropriately accounted for and discussed in detail within the test campaign.

As a final note, as mentioned earlier, our system has been rigorously tested in complex environments, accounting for multipath effects and noise, with all errors included in our simulations. As long as the communication link between the user and the positioning system is not completely obstructed, the system performs well. In scenarios where the link is fully blocked, the system defaults to the last known location. If the user moves during this period, slight errors may occur until the communication link is reestablished. If the user remains stationary, the reported location remains accurate.

#### A. Optimal Placement Algorithm Assessment

By displaying performance results and contrasting them with a benchmark that ignores the optimal placement, the usefulness of our suggested optimization algorithm is evaluated.

Because the primary goal is to identify the optimal placement of follower oscillators, the solution is entirely dependent on the dimensions of the room (i.e., the provided floor plan). As a result, we devised our algorithm to take the floor plan as input and produce the optimal placement of the oscillators as output.

The effectiveness of the algorithm is evaluated on three distinct floor plans to showcase its adaptability to different

TABLE II  
FOLLOWER OSCILLATOR PLACEMENT FOR DIFFERENT ROOM SIZES WITH OPTIMAL SOLUTION

Room Dimensions	Osc. # 1	Osc. # 2	Osc. # 3	Osc. # 4
Office Room (5 m × 5 m × 4 m)	(0,1,2)	(5,1,2)	(5,5,3)	(2,2,4)
Conference Room (10 m × 10 m × 4 m)	(7,3,4)	(6,1,4)	(0,9,4)	(8,0,2)
Game Room (20 m × 20 m × 4 m)	(19,10,4)	(3,8,4)	(8,20,3)	(2,0,2)

TABLE III  
FOLLOWER OSCILLATOR PLACEMENT FOR DIFFERENT ROOM SIZES WITH A CONVENTIONAL CONFIGURATION TO BENCHMARK THE OPTIMAL SOLUTION

Room Dimensions	Osc. # 1	Osc. # 2	Osc. # 3	Osc. # 4
Office Room (5 m × 5 m × 4 m)	(3,4,4)	(3,2,4)	(3,1,4)	(4,1,4)
Conference Room (10 m × 10 m × 4 m)	(6,10,4)	(2,7,4)	(3,7,4)	(7,1,4)
Game Room (20 m × 20 m × 4 m)	(18,10,4)	(14,3,4)	(19,11,4)	(14,1,4)

room dimensions, ranging from modest to extremely large sizes. The first example involves a typical office room measuring 5 m × 5 m × 4 m acts as an example for playing virtual games on VR devices. The second example is a large conference room with dimensions of 10 m × 10 m × 4 m, which is suitable for AR applications in larger setups. Lastly, the algorithm is put to the test on an extreme example, a large game room measuring 20 m × 20 m × 4 m that can accommodate multiuser AR/VR games, such as laser tag.

Fig. 8 compares the  $G(\cdot)$  values of optimal and nonoptimal conventional placements. Nonoptimized configurations and the optimal placements are listed in Tables II and III, respectively, where all the numbers are demonstrated in meters.

As shown in the figure, the algorithm consistently produces satisfactory results across all scenarios tested. Furthermore, the provided figure emphasizes the importance of using the proposed optimization algorithm for follower oscillator placement rather than a conventional approach, due to the significant impact of  $G(x, y, z)$  values on overall accuracy. It should be noted that the values of  $G(x, y, z)$  differ for each  $(x, y, z)$  point in the room. As a result, displaying values for all points in three dimensions necessitates a 4-D plot. To avoid this, in Fig. 8, we take an average of all the  $z$  planes and display the final result on the  $X - Y$  plane. The proposed algorithm is expected to perform well, particularly for smaller dimensions. However, it demonstrated its ability to generate optimal solutions in a timely manner even for significantly larger dimensions.

Fig. 9 presents the cumulative distribution function (CDF) of  $G(\cdot)$  values for the optimal placement in the mentioned three distinct indoor environments. These optimal placements are enumerated in Table II. The principal aim of the analysis in this figure is to demonstrate the number of points in set  $\mathbb{U}$  that have  $G(x, y, z)$  values lower than a specific threshold. The optimization problem's objective was to guarantee that the majority of the points had their  $G(x, y, z)$  lower than 20. We set a threshold of 20 given the system's accuracy in providing distance information and the requirement to keep overall 3-D

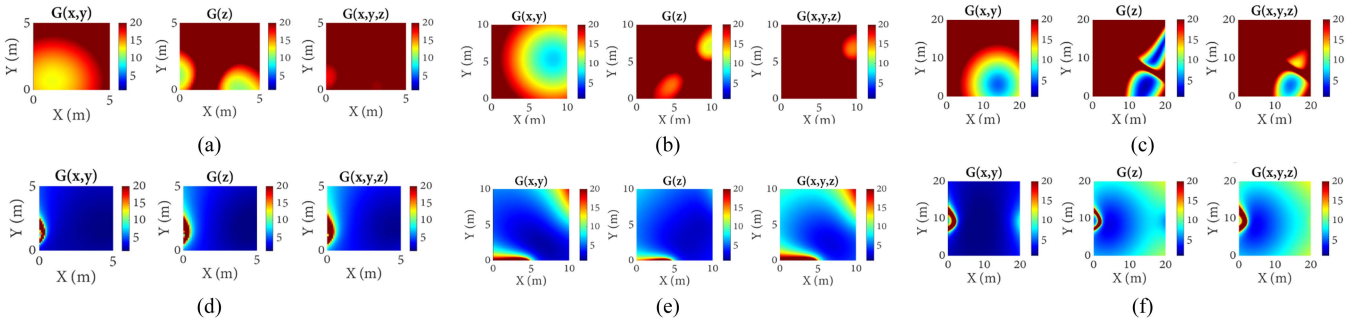


Fig. 8. Illustration of  $G(\cdot)$  values comparison between the baseline and optimal placement for various indoor space dimensions. (a) Baseline configuration for an office room. (b) Baseline configuration for a conf. room (c) Baseline configuration for a game room. (d) Optimal configuration for an office room. (e) Optimal configuration for a conf. room. (f) Optimal configuration for a game room.

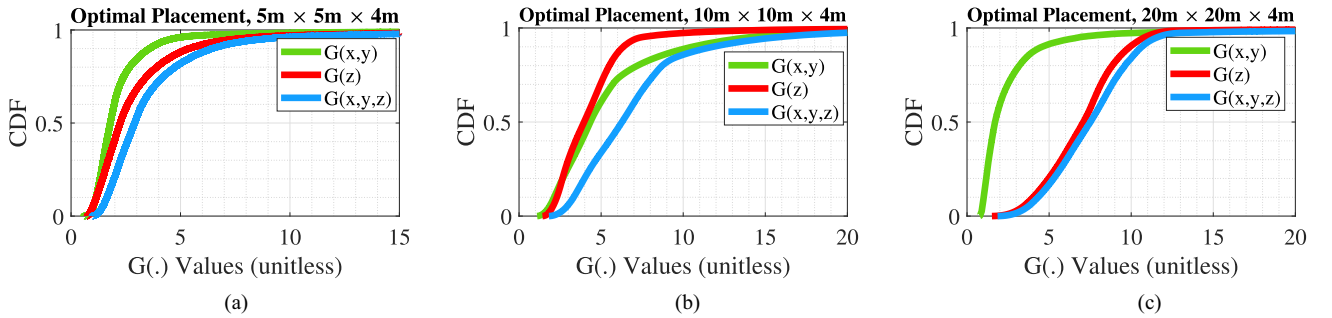


Fig. 9. CDF plot representation of  $G(\cdot)$  values for various room dimensions with optimal configuration shown in Table II.

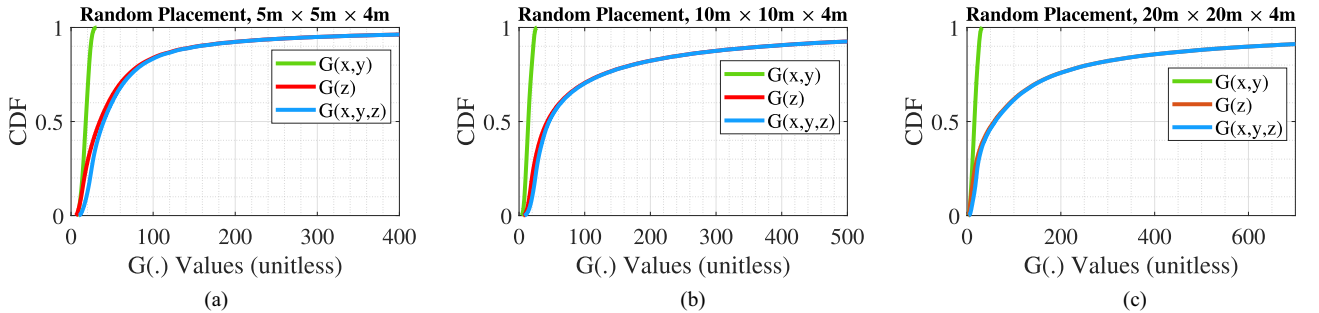


Fig. 10. CDF plot representation of  $G(\cdot)$  values for various room dimensions with nonoptimal conventional configuration represented in Table III.

accuracy below 1 mm. As depicted in the figure, this objective has been attained for all the scenarios.

For instance, in a typical office room, more than 95% of the points in  $\mathbb{U}$  have  $G(x, y, z)$  values less than 8. In the case of a large conference room, this value is 14, and for a large game room, it is 12. These values are all below 20, confirming that the proposed optimization framework performed as anticipated.

In order to establish a benchmark and underscore the crucial nature of optimal placement requirements, we present in Fig. 10 the identical plots as depicted in Fig. 9, except with a nonoptimal placement configuration, as listed in Table III. As can be observed in this figure, the  $G(x, y, z)$  values surge to several hundred, rather than being predominantly below 20 for

the majority of the points in set  $\mathbb{U}$ . This implies that even if a highly precise system is employed to measure time (and, by extension, distance), the final 3-D accuracy may be unreliable owing to the large  $G(x, y, z)$  values.

### B. Final Assessment

Our study has three main goals. To begin, we propose a novel method for measuring time with high precision using isochrons in photonic oscillators. The accuracy is determined by the oscillation frequency as well as the resolution of the oscillation cycle in terms of isochrons. As shown in Fig. 11, the accuracy of the phase shift measurement induced by an incoming pulse is proportional to the number of cycles  $k$  required for the

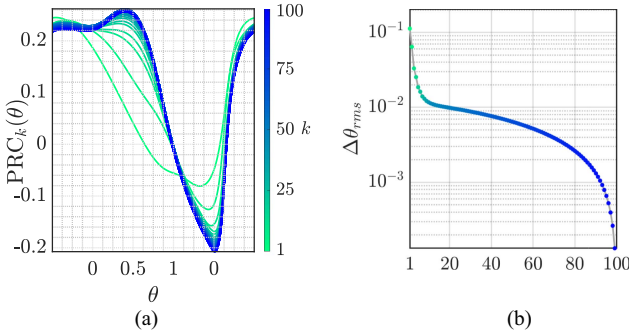


Fig. 11. (a) Each  $\text{PRC}_k(\theta)$  indicates the phase response of the system to an external excitation of fixed amplitude for varying relaxation intervals corresponding to integer multiples of  $T_{1c}$ , i.e.,  $kT_{1c}$ . (b) Root-mean-square error of the phase response for varying relaxation intervals.

excitation to relax on the system's stable limit cycle. The spatial resolution  $\Delta x_{\text{rms}}$  is proportional to the phase measurement error  $\Delta\theta_{\text{rms}}$  as

$$\Delta x_{\text{rms}} = \Delta\theta_{\text{rms}} \frac{c}{f_{1c}} \quad (22)$$

where the first term clearly demonstrates the benefit of measuring the phase within a cycle versus measuring whole cycles. As an example, for  $f_{1c} = 3$  GHz or  $f_{1c} = 30$  GHz the spatial resolution due to time measurement is  $\Delta x_{\text{rms}} = 10^{-4}$  m or  $\Delta x_{\text{rms}} = 10^{-5}$  m for a  $\Delta\theta_{\text{rms}} = 10^{-3}$  achieved after  $k \simeq 50$  cycles corresponding to a negligible time span, smaller than  $10^{-8}$  s.

Second, we look into the viability of using injection-locking technology to achieve precise clock synchronization, which is critical for TDoA systems. For the clock synchronization, the nonlinear characteristic of the synchronization mechanism ensures an exponential convergence rate and a precise phase locking of the receivers' clocks as presented in Fig. 5(c) and (d). Finally, we improve 3-D localization accuracy by introducing  $G(x, y, z)$  and creating an optimization framework to reduce geometry-induced error in overall location estimation.

The CDF of localization accuracy with the optimal placement is shown in Fig. 12, which is based on Table II. As shown in the figure, regardless of the environment's dimensions, an overall 3-D accuracy of less than 1 mm is achieved. These plots are created using the parameter values discussed in Section IV core, which were used to develop our system.

To establish a baseline, we show nonoptimized placement configurations in Fig. 13, as listed in Table III. These plots can be compared to the optimal plots shown in Fig. 12. The 3-D error increases to 1 cm in the nonoptimized case, but remains primarily below 1 mm in the optimized case. This emphasizes the importance of proper anchor placements.

We plot the localization accuracy for different lasers' realistic parameter values using our optimal placement approach, in Fig. 14. The frequency of the limit cycle  $f_{1c}$  and the phase measurement error  $\Delta\theta_{\text{rms}}$  are of particular interest. Smaller values for  $f_{1c}$  result in performance degradation, as shown in Fig. 14(a). When we change the  $f_{1c} = 30$  GHz to  $f_{1c} = 3$  GHz for a fixed

value of  $\Delta\theta_{\text{rms}} = 10^{-3}$ , the localization error increases from 1 mm to 1 cm. This gives us design flexibility in determining the frequency of the limit cycle based on the use case. Higher frequencies are better suited for applications requiring greater localization accuracy (sub-1 mm), such as finger tracking. Lower frequencies, on the other hand, can be used for applications requiring sub-cm accuracy, such as autonomous indoor navigation of drones in large warehouses. Furthermore, in Fig. 14(b), we investigate the tradeoff between the system's update rate and the overall accuracy: waiting for longer cycles enhances the overall accuracy; for instance,  $k > 50$ , which is the plot with  $\Delta\theta_{\text{rms}} = \frac{1}{2} \times 10^{-3}$ . This means that the update rate will be slowed by a few nanoseconds. Longer relaxation times, in general, result in better resolution for phase measurements, which leads to better overall 3-D accuracy. As shown in Fig. 11(b), increasing the relaxation time to a hundred cycles ( $k = 100$ ) improves phase shift resolution significantly ( $\Delta\theta_{\text{rms}} = 10^{-5}$ ), which is hundred times better than  $k = 50$ . This means that for lower frequencies, we can achieve high-accuracy localization by using a longer relaxation time (slightly slower update rate).

## IX. DISCUSSION

In summary, in this work, we aim to enhance the localization error inherent in ranging-based techniques by introducing a novel photonic timing mechanism combined with an injection-locking technique. This photonic timing allows for ultra-high-resolution time measurements, leading to high-accuracy distance estimations, marking the first contribution of IsoPos. The second contribution is the high-accuracy synchronization achieved through the photonic injection-locking mechanism. In our final contribution, unlike the majority of existing literature that primarily focuses on ranging-based errors, we comprehensively investigate all sources of error and offer solutions to mitigate geometry-induced errors.

Accurate localization requires precise distance information to mitigate significant errors when utilizing a trilateration system that converts distances into locations; hence, precise timing is crucial. To the best of the authors' knowledge, our proposal of a timing mechanism based on the isochronous structure of photonic oscillators is unprecedented. Prior studies have focused on enhancing localization accuracy mainly by modifying the signal modulation [9] or increasing bandwidth for improved timing and distance resolution [29].

Generally, existing literature [8], [29], [57] tends to minimize the adverse impact of channels on signal reception, relying on the system's inherent capacity for distance estimation, such as those provided in 5G New Radio [29] or Wireless Fidelity positioning [57], without delving into the potential for systemic improvements in timing mechanisms for more accurate distance measurements. Our approach targets the fundamental issue of distance estimation mechanisms. By introducing a novel timing mechanism based on the isochronous structure of photonic oscillators, we aim to fundamentally enhance overall system performance. In addition, our assumptions are grounded in reality. Achieving high-accuracy synchronization between

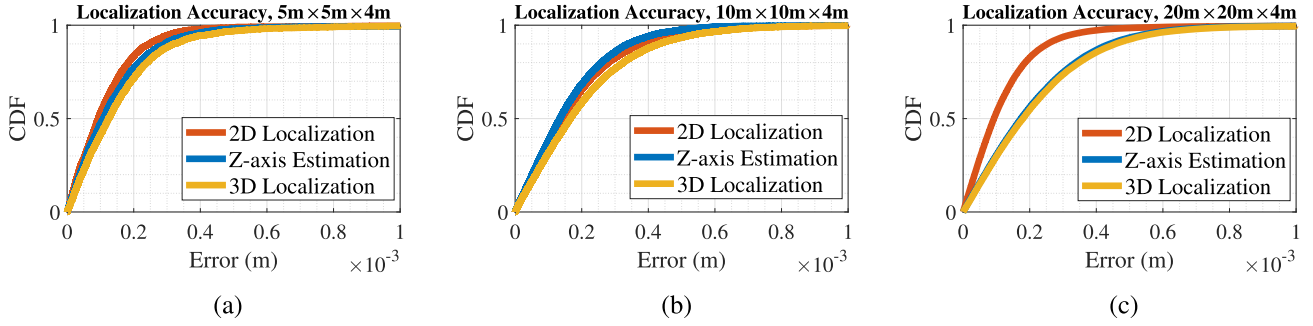


Fig. 12. CDF plots representation of 2-D and 3-D and localization accuracy as well as the Z-axis estimation for various room dimensions with the optimal configuration shown in Table II.

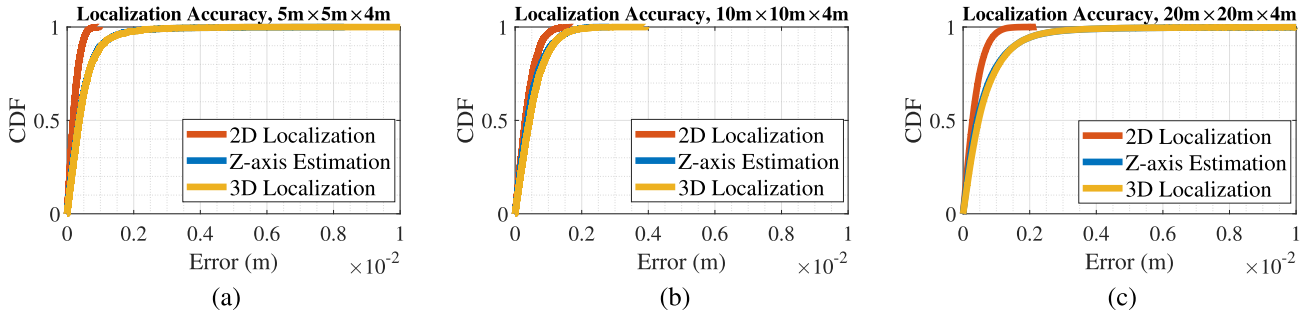


Fig. 13. CDF plots representation of 2-D and 3-D localization accuracy as well as the Z-axis estimation for various room dimensions with a nonoptimized configuration shown in Table III.

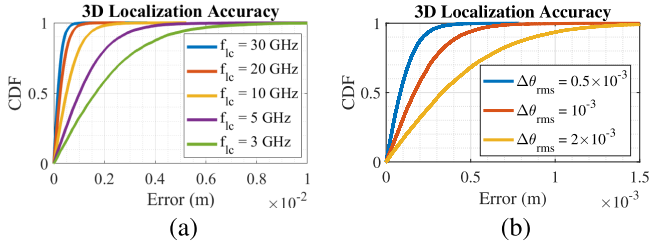


Fig. 14. 3-D localization accuracy evaluations for different laser's parameter values. (a) Effect of  $f_{ic}$  for the fixed value of  $\Delta\theta_{rms} = 10^{-3}$  ( $k \simeq 50$  cycles). (b) Effect of  $\Delta\theta_{rms}$  for the fixed value of  $f_{ic} = 30$  GHz.

users and positioning nodes is challenging in wireless systems; thus, we suggest employing a TDoA system for final location determination. A significant challenge in TDoA localization is the synchronization among positioning nodes themselves, where minor drifts can lead to substantial errors. To counter this, we propose an injection-locking technique that ensures highly accurate synchronization among the positioning nodes through a leader–follower design.

The majority of research presented in the literature [8], [9], [21], [57] reports final 3-D localization accuracies ranging from tens of centimeters [21] to a meter or more [57]. This limitation is primarily due to the inherent constraints of the system's timing resolution capabilities. In contrast, by proposing a fundamental shift in the method of time measurement, we can enhance this accuracy to millimeter-level precision.

## X. CONCLUSION AND FUTURE WORK

*Conclusion:* In this article, we propose a novel positioning system, named IsoPos, that utilizes ideas from tunable photonic oscillators and their isochrons' structure to enhance localization accuracy. To that end, we introduce IPT mechanism, a novel approach for measuring the ToA with extremely high resolution. IPT exploits the phase shift in the receiver's oscillation—determined by its isochrons' structure—induced by excitation pulses. To attain precise synchronization among different positioning nodes, which is a challenge in current localization architectures, we propose ILS protocol, which employs the injection locking of tunable photonic oscillators. In addition, we present an optimization framework to mitigate the adverse impact of geometry on location accuracy. Our comprehensive numerical results show that the proposed system achieves sub-1 mm 3-D localization accuracy across different scenarios.

*Future work:* The chief goal of this work was to introduce a novel high-resolution ToA measurement and precise time synchronization approach. These were the foundational elements of our proposed positioning system. We intend to focus our future research primarily on the RF transmission aspect and investigate the possibility of mitigating potential channel-induced negative impacts, such as multipath, noise, and interference, through the robust selection of  $s(t)$ . With that objective in mind, we plan to examine the most effective design of  $s(t)$  as well as the feasibility of using non-LoS information in large-scale scenarios. This is significant when the existence of LoS is uncertain. Furthermore,

we are developing a testbed that will include quantum well and external cavity lasers. The end goal we aim to achieve is the development of a chip-level model that can confirm the effectiveness of the suggested system in practical situations, such as delivering accurate hand-tracking for AR glasses.

## REFERENCES

- [1] Y. Wang, Y. Ren, Y. Chen, and J. Yang, "Wi-mesh: A WiFi vision-based approach for 3D human mesh construction," in *Proc. 20th ACM Conf. Embedded Netw. Sens. Syst.*, New York, NY, USA, 2023, pp. 362–376. [Online]. Available: <https://doi.org/10.1145/3560905.3568536>
- [2] L.-W. Chen, H.-W. Huang, and C.-Y. Cho, "Anchor-few: An adaptive precise indoor positioning system for low anchor densities based on IoT localization," in *Proc. 28th Annu. Int. Conf. Mobile Comput. Netw.*, New York, NY, USA, 2022, pp. 835–837. [Online]. Available: <https://doi.org/10.1145/3495243.3558254>
- [3] A. Famili, V. Slyusar, Y. H. Lee, and A. Stavrou, "Vehicular teamwork for better positioning," in *Proc. IEEE Int. Conf. Syst. Man Cybern.*, 2023, pp. 3507–3513.
- [4] A. Adeyeye, C. Lynch, J. Hester, and M. Tentzeris, "A machine learning enabled mmWave RFID for rotational sensing in human gesture recognition and motion capture applications," in *Proc. IEEE/MTT-S Int. Microw. Symp.*, 2022, pp. 137–140.
- [5] F. DAVIS, C.-F. Chiasserini, L. Musumeci, and C. Borgiattino, "Context-aware peer-to-peer and cooperative positioning," in *Proc. Int. Conf. Localization*, 2014, pp. 1–6.
- [6] A. Canals, P. Josephy, S. Tanner, and R. Wattenhofer, "Robust indoor localization with ADS-B," in *Proc. 27th Annu. Int. Conf. Mobile Comput. Netw.*, New York, NY, USA, 2021, pp. 505–516. [Online]. Available: <https://doi.org/10.1145/3447993.3483257>
- [7] S. Han et al., "MEgATrack: Monochrome egocentric articulated hand-tracking for virtual reality," *ACM Trans. Graph.*, vol. 39, no. 4, Aug. 2020. [Online]. Available: <https://doi.org/10.1145/3386569.3392452>
- [8] W. Mao, J. He, and L. Qiu, "CAT: High-precision acoustic motion tracking," in *Proc. 22nd Annu. Int. Conf. Mob. Comput. Netw.*, New York, NY, USA, 2016, pp. 69–81. [Online]. Available: <https://doi.org/10.1145/2973750.2973755>
- [9] A. Famili, A. Stavrou, H. Wang, and J.-M. J. Park, "PILOT: High-precision indoor localization for autonomous drones," *IEEE Trans. Veh. Technol.*, vol. 72, no. 5, pp. 6445–6459, May 2022.
- [10] S. E. Trevlakis et al., "Localization as a key enabler of 6G wireless systems: A comprehensive survey and an outlook," *IEEE Open J. Commun. Soc.*, vol. 4, pp. 2733–2801, 2023.
- [11] A. T. Winfree, *The Geometry of Biological Time*. New York, NY, USA: Springer, 1980.
- [12] A. Pikovsky, M. Rosenblum, and J. Kurths, *Synchronization: A Universal Concept in Nonlinear Sciences*. Cambridge, U.K.: Cambridge Univ. Press, 2001.
- [13] E. M. Izhikevich, *Dynamical Systems in Neuroscience: The Geometry of Excitability and Bursting*. Cambridge MA, USA: MIT Press, 2007.
- [14] G. Himona, V. Kovanis, and Y. Kominis, "Isochrons, phase response and synchronization dynamics of tunable photonic oscillators," *Phys. Rev. Res.*, vol. 4, 2022, Art. no. L012039.
- [15] G. Himona, V. Kovanis, and Y. Kominis, "Time crystals transforming frequency combs in tunable photonic oscillators," *Chaos Interdiscipl. J. Nonlinear Sci.*, vol. 33, no. 4, 2023, Art. no. 043134.
- [16] R. Sakuraba, K. Iwakawa, K. Kanno, and A. Uchida, "Tb/s physical random bit generation with bandwidth-enhanced chaos in three-cascaded semiconductor lasers," *Opt. Exp.*, vol. 23, 2015, Art. no. 1490.
- [17] T. K. Parašo et al., "A modulator-free quantum key distribution transmitter chip," *Npj Quantum Inf.*, vol. 4, 2019, Art. no. 42.
- [18] Y. Lo et al., "Self-tuning transmitter for quantum key distribution using machine intelligence," *Phys. Rev. Appl.*, vol. 18, Sep. 2022, Art. no. 034087. [Online]. Available: <https://link.aps.org/doi/10.1103/PhysRevApplied.18.034087>
- [19] H. Ryden et al., "Baseline performance of LTE positioning in 3GPP 3D MIMO indoor user scenarios," in *Proc. Int. Conf. Localization GNSS*, 2015, pp. 1–6.
- [20] L. Bai et al., "Computer vision-based localization with visible light communications," *IEEE Trans. Wireless Commun.*, vol. 21, no. 3, pp. 2051–2065, Mar. 2022.
- [21] A. Famili, A. Stavrou, H. Wang, and J.-M. Park, "iDROP: Robust localization for indoor navigation of drones with optimized beacon placement," *IEEE Internet Things J.*, vol. 10, no. 16, pp. 14226–14238, Aug. 2023.
- [22] X. Tong, Y. Wan, Q. Li, X. Tian, and X. Wang, "CSI fingerprinting localization with low human efforts," *IEEE/ACM Trans. Netw.*, vol. 29, no. 1, pp. 372–385, Feb. 2021.
- [23] Z. Zhu, C. Guo, R. Bao, M. Chen, W. Saad, and Y. Yang, "Positioning using visible light communications: A perspective arcs approach," *IEEE Trans. Wireless Commun.*, vol. 22, no. 10, pp. 6962–6977, Oct. 2023.
- [24] A. Famili, A. Stavrou, H. Wang, and J.-M. J. Park, "RAIL: Robust acoustic indoor localization for drones," in *Proc. IEEE 95th Veh. Technol. Conf. (VTC2022-Spring)*, 2022, pp. 1–6.
- [25] Y. Hu et al., "Experience: Practical indoor localization for malls," in *Proc. 28th Ann. Int. Conf. Mobile Comput. Netw.*, New York, NY, USA, 2022, pp. 82–93. [Online]. Available: <https://doi.org/10.1145/3495243.3517021>
- [26] J. Ni et al., "Experience: Pushing indoor localization from laboratory to the wild," in *Proc. 28th Annu. Int. Conf. Mobile Comput. Netw.*, New York, NY, USA, 2022, pp. 147–157. [Online]. Available: <https://doi.org/10.1145/3495243.3560546>
- [27] A. Famili and J.-M. J. Park, "ROLATIN: Robust localization and tracking for indoor navigation of drones," in *Proc. IEEE Wireless Commun. Netw. Conf.*, 2020, pp. 1–6.
- [28] X. Wang, X. Wang, S. Mao, J. Zhang, S. C. G. Periaswamy, and J. Patton, "Adversarial deep learning for indoor localization with channel state information tensors," *IEEE Internet Things J.*, vol. 9, no. 19, pp. 18182–18194, Oct. 2022.
- [29] A. Famili, T. Atalay, A. Stavrou, H. Wang, and J.-M. Park, "OFDRA: Optimal femtocell deployment for accurate indoor positioning of RIS-mounted AVs," *IEEE J. Sel. Areas Commun.*, vol. 41, no. 12, pp. 3783–3798, Dec. 2023.
- [30] B. Zhu, J. Cheng, Y. Wang, J. Yan, and J. Wang, "Three-dimensional VLC positioning based on angle difference of arrival with arbitrary tilting angle of receiver," *IEEE J. Sel. Areas Commun.*, vol. 36, no. 1, pp. 8–22, Jan. 2018.
- [31] G. Himona, A. Famili, A. Stavrou, V. Kovanis, and Y. Kominis, "Isochrons in tunable photonic oscillators and applications in precise positioning," in *Proc. Phys. Simul. Optoelectron. Devices*, 2023, Art. no. 124150E. [Online]. Available: <https://doi.org/10.1117/12.2648977>
- [32] L. A. Coldren, S. W. Corzine, and M. L. Masanovic, *Diode Lasers and Photonic Integrated Circuits*. Hoboken, NJ, USA: Wiley, 2012.
- [33] T. Komljenovic, D. Huang, P. Pintus, M. A. Tran, M. L. Davenport, and J. E. Bowers, "Photonic integrated circuits using heterogeneous integration on silicon," *Proc. IEEE*, vol. 106, no. 12, pp. 2246–2257, Dec. 2018.
- [34] D. J. Herrera, K. Tomkins, C. Valagiannopoulos, V. Kovanis, and L. F. Lester, "Strongly detuned tunable photonic oscillators," *IEEE Photon. Technol. Lett.*, vol. 33, no. 24, pp. 1399–1402, 2021.
- [35] Y. Kominis, A. Bountis, and V. Kovanis, "Radically tunable ultrafast photonic oscillators via differential pumping," *J. Appl. Phys.*, vol. 127, 2020, Art. no. 083103.
- [36] O. Suvak and A. Demir, "Quadratic approximations for the isochrons of oscillators: A general theory, advanced numerical methods, and accurate phase computations," *IEEE Trans. Comput.-Aided Des. Integr. Circuits Syst.*, vol. 29, no. 8, pp. 1215–1228, Aug. 2010.
- [37] O. Suvak and A. Demir, "On phase models for oscillators," *IEEE Trans. Comput.-Aided Des. Integr. Circuits Syst.*, vol. 30, no. 7, pp. 972–985, Jul. 2011.
- [38] A. Famili, G. Himona, Y. Kominis, A. Stavrou, and V. Kovanis, "Isochrons in photonic oscillators: A paradigm shift in positioning," in *Proc. IFIP Netw. Conf.*, Thessaloniki, Greece, Jun. 2024, pp. 1–7.
- [39] N. Rajagopal, "Localization, beacon placement and mapping for range-based indoor localization systems," Ph.D. dissertation, Dept. Elect. Comput. Eng., Carnegie Mellon Univ., Pittsburgh, PA, USA, Aug. 2019.
- [40] A. Famili, T. Atalay, A. Stavrou, and H. Wang, "Wi-six: Precise positioning in the metaverse via optimal Wi-Fi router deployment in 6G networks," in *Proc. IEEE Int. Conf. Metaverse Comput. Netw. Appl.*, 2023, pp. 17–24.
- [41] R. Sharma and V. Badarla, "Analysis of a novel beacon placement strategy 3D localization in indoor spaces," in *Proc. 11th Int. Conf. Commun. Syst. Netw.*, Jan. 2019, pp. 320–327.
- [42] N. Patwari, A. O. Hero, M. Perkins, N. S. Correal, and R. J. O'Dea, "Relative location estimation in wireless sensor networks," *IEEE Trans. Signal Process.*, vol. 51, no. 8, pp. 2137–2148, Aug. 2003.
- [43] A. Famili, S. Sun, T. O. Atalay, and A. Stavrou, "Precision tracking in geofencing systems using deep reinforcement learning," in *Proc. IEEE Int. Performance, Comput. Commun. Conf.*, Orlando, USA, Nov. 2024, p. 10.

- [44] W. Dai, Y. Shen, and M. Z. Win, "A computational geometry framework for efficient network localization," *IEEE Trans. Inf. Theory*, vol. 64, no. 2, pp. 1317–1339, Feb. 2018.
- [45] T. Wang, Y. Shen, A. Conti, and M. Z. Win, "Network navigation with scheduling: Error evolution," *IEEE Trans. Inf. Theory*, vol. 63, no. 11, pp. 7509–7534, Nov. 2017.
- [46] A. Famili, A. Stavrou, H. Wang, and J.-M. J. Park, "SPIN: Sensor placement for indoor navigation of drones," in *Proc. IEEE Latin-Amer. Conf. Commun.*, 2022, pp. 1–6.
- [47] H. Wang, N. Rajagopal, A. Rowe, B. Sinopoli, and J. Gao, "Efficient beacon placement algorithms for time-of-flight indoor localization," in *Proc. 27th ACM SIGSPATIAL Int. Conf. Adv. Geograph. Inf. Syst.*, New York, NY, USA, 2019, pp. 119–128. [Online]. Available: <https://doi.org/10.1145/3347146.3359344>
- [48] J. Schmalenstroerer and R. Haeb-Umbach, "Investigations into Bluetooth low energy localization precision limits," in *Proc. 24th Eur. Signal Process. Conf.*, Aug. 2016, pp. 652–656.
- [49] A. Famili, A. Stavrou, H. Wang, and J.-M. J. Park, "OPTILOD: Optimal beacon placement for high-accuracy indoor localization of drones," *Sensors*, vol. 24, no. 6, 2024. [Online]. Available: <https://www.mdpi.com/1424-8220/24/6/1865>
- [50] N. Rajagopal, S. Chayapathy, B. Sinopoli, and A. Rowe, "Beacon placement for range-based indoor localization," in *Proc. Int. Conf. Indoor Positioning Indoor Navigation*, Oct. 2016, pp. 1–8.
- [51] T. Erneux and P. Glorieux, *Laser Dynamics*. Cambridge, U.K.: Cambridge Univ. Press, 2010.
- [52] S. Wieczorek, B. Krauskopf, T. B. Simpson, and D. Lenstra, "The dynamical complexity of optically injected semiconductor lasers," *Phys. Rep.*, vol. 416, pp. 1–128, 2005.
- [53] A. Mauroy and I. Mezić, "On the use of fourier averages to compute the global isochrons of (quasi) periodic dynamics," *Chaos: An Interdiscipl. J. Nonlinear Sci.*, vol. 22, no. 3, 2012, Art. no. 033112.
- [54] W. Mao, Z. Zhang, L. Qiu, J. He, Y. Cui, and S. Yun, "Indoor follow me drone," in *Proc. 15th Annu. Int. Conf. Mobile Syst., Appl., Serv.*, New York, NY, USA, 2017, pp. 345–358. [Online]. Available: <https://doi.org/10.1145/3081333.3081362>
- [55] A. Famili and A. Stavrou, "CARTA: Coordinated arrangement of receivers for target acquisition," in *Proc. IFIP Netw. Conf.*, 2024, pp. 323–331.
- [56] D. Simon, *Evolutionary Optimization Algorithms*. Hoboken, NJ, USA: Wiley, 2013.
- [57] E. Soltanaghahi et al., "Millimetro: mmWave retro-reflective tags for accurate, long range localization," in *Proc. 27th Annu. Int. Conf. Mobile Comput. Netw.*, New York, NY, USA, 2021, pp. 69–82. [Online]. Available: <https://doi.org/10.1145/3447993.3448627>